Journal of
Applied
Crystallography

ISSN 1600-5767

Received 20 September 2013
Accepted 15 April 2014

High-resolution X-ray diffraction investigation on the evolution of the substructure of individual austenite grains in TRIP steels during tensile deformation

Romain Blondé,[a,b]* Enrique Jimenez-Melero,[c] Richard Huizenga,[d] Lie Zhao,[b,d] Jonathan Wright,[e] Ekkes Brück,[a] Sybrand van der Zwaag[f] and Niels van Dijk[a]

[a]Fundamental Aspects of Materials and Energy, Delft University of Technology, Mekelweg 15, Delft, 2629 JB, The Netherlands, [b]Materials innovation institute, Mekelweg 2, Delft, 2628 CD, The Netherlands, [c]Dalton Cumbrian Facility, Westlakes Science and Technology Park, The University of Manchester, Moor Row, Cumbria CA24 3HA, UK, [d]Department of Materials Science and Engineering, Delft University of Technology, Mekelweg 2, Delft, 2628 CD, The Netherlands, [e]European Synchrotron Radiation Facility, BP-220, Grenoble, France, and [f]Novel Aerospace Materials Group, Delft University of Technology, Kluyverweg 1, Delft, 2629 HS, The Netherlands. Correspondence e-mail: r.j.p.blonde@tudelft.nl

The martensitic transformation behaviour of the metastable austenite phase in low-alloyed transformation-induced plasticity (TRIP) steels has been studied *in situ* using high-energy X-ray diffraction during deformation. The austenite stability during tensile deformation has been evaluated at different length scales. A powder diffraction analysis has been performed to correlate the macroscopic behaviour of the material to the observed changes in the volume phase fraction. Moreover, the austenite deformation response has been studied at the length scale of individual grains, where an in-depth characterization of four selected grains has been performed, including grain volume, local carbon concentration and grain orientation. For the first time, a high-resolution far-field detector was used to study the initial and evolving structure of individual austenite grains during uniaxial tensile deformation. It was found that the austenite subgrain size does not change significantly during tensile deformation. Most austenite grains show a complete martensitic transformation in a single loading step.

1. Introduction

In situ high-energy synchrotron X-ray diffraction (XRD) is a powerful tool to study the fundamentals of phase transformations. The intense beam of high-energy X-rays makes it possible to monitor the change in phase fraction and lattice parameters of the constituent phases in the bulk of a material (Militzer, 2002). Using this unique capability it is possible to analyse the transformation behaviour of metastable austenite in low-alloyed multiphase steels (Blondé *et al.*, 2012; Jimenez-Melero *et al.*, 2007*a*). By selecting an optimal beam size the austenite phase can be characterized as a powder average and at the level of individual austenite grains.

The transformation of metastable austenite into martensite during deformation makes it possible to achieve greater elongations and lends these steels their excellent combination of strength and ductility. This mechanism is known as the transformation-induced plasticity (TRIP) effect. This phenomenon increases the work-hardening rate during plastic deformation and hence delays necking (Dan *et al.*, 2007; Jacques *et al.*, 2007). This has opened the door to obtaining outstanding combinations of strength and ductility. At room temperature, a typical low-alloyed TRIP steel microstructure contains three phases: ferrite, bainite and metastable austenite (Timokhina *et al.*, 2004; Zaefferer *et al.*, 2004). In our previous synchrotron X-ray diffraction studies we have monitored the transformation behaviour of metastable austenite in low-alloyed TRIP steels during tensile deformation at room temperature (Jimenez-Melero *et al.*, 2011) and during cooling to a temperature of 100 K (Jimenez-Melero *et al.*, 2007*a*,*b*, 2009; van Dijk *et al.*, 2005). We found that the austenite stability depends on the local carbon content, the grain size and the orientation.

In this study, a detailed characterization of four individual austenite grains has been performed from a high-resolution X-ray diffraction experiment using a far-field detector. In order to evaluate their mechanical stability during tensile deformation, first the average behaviour of the austenite fraction has been analysed using a medium-field powder diffraction approach (the term near-field is reserved for cases where the detector is placed as close as possible behind the sample). Medium-field measurements covering a wide angular rotation range probing a lower angular resolution have been

performed. These data have been analysed using the three-dimensional XRD (3DXRD) method (Schmidt *et al.*, 2003; Oddershede *et al.*, 2010; Bernier *et al.*, 2011; Edmiston *et al.*, 2011; Poulsen, 2004) in order to characterize the transformation behaviour of the four retained austenite grains in terms of grain size, local carbon content and grain orientation.

For TRIP steels it is an open question whether plastic deformation (*i.e.* the creation of dislocations or dislocation networks) precedes the martensite transformation or the martensite forms from plastically undeformed austenite grains. So far, no experimental single-grain data have been available to resolve this question. To monitor the material at smaller length scales, an additional high-resolution far-field detector was used. For the first time, the subgrain structure of austenite prior to the transformation has been observed. The use of high-resolution diffraction to monitor subgrains under tensile load was previously explored by Jakobsen *et al.* (2007, 2006) in pure metals. This method is nondestructive, in contrast to the conventional methods to study the subgrain structure within a single grain, like electron backscatter diffraction (Humphreys, 2001; Jiang *et al.*, 2013) and transmission electron microscopy (Huang *et al.*, 2001; Dalla Torre *et al.*, 2004). The interplay between tensile deformation, the orientation-dependent austenite-to-martensite transformation, grain volume and carbon concentration has been analysed using diffraction data from the medium-field detector, while the substructure evolution of individual grains as a function of the macroscopic stress has been investigated using diffraction data from the far-field detector. The analysis from the combination of data from both medium-field and far-field detectors provided a detailed characterization of the austenite stability. While the angular resolution obtained with the far-field detector is very high, the spatial resolution is limited (either to the beam size or to a smaller value defined by reconstruction of the reflections on the medium-field detector).

2. Experimental details

2.1. Sample preparation

The chemical composition of the studied TRIP steel is shown in Table 1. A cylindrical dog-bone tensile specimen with a gauge length of 10 mm and a diameter of 1 mm was machined from hot-rolled sheet material. The cylindrical axis of the samples was chosen parallel to the rolling direction (RD). A mark parallel to the normal direction of the sheet material was made on the top part of the cylindrical sample in order to keep track of the normal (ND) and transverse (TD) sample orientation. First, the sample was annealed in a salt bath for 30 min at an intercritical temperature of 1143 K in order to obtain equal fractions of austenite and ferrite. Then the sample was quenched in a second salt bath to a temperature of 673 K and held for 2 min. During this holding time part of the intercritical austenite transformed into bainite and the remaining austenite was enriched in carbon. The carbon-enriched austenite remained in a metastable state after a final water quench to room temperature. This heat treatment, discussed in more detail in a previous study (Blondé *et al.*, 2011), yielded a multiphase microstructure composed of ferrite (α), bainite (α_b) and metastable austenite (γ), as shown in the optical micrograph of Fig. 1. The austenite phase is present in two forms: blocky type and film type. The blocky type (with a size > 1 µm) corresponds to the metastable retained austenite, while the film type (with a size < 1 µm) corresponds to the stable austenite present within the bainite. The stability of these blocky-type austenite grains defines the TRIP effect, as the film-type austenite remains stable during tensile deformation. The austenite grain size distribution was investigated previously (Jimenez-Melero *et al.*, 2007*b*).

Table 1
Chemical composition of the TRIP steel in wt% with balance Fe.

C	Mn	Si	Al	P
0.218	1.539	0.267	1.75	0.018

2.2. Experimental setup

The *in situ* high-energy XRD experiments were performed with the three-dimensional X-ray diffraction microscope at the ID11 beamline of the European Synchrotron Radiation Facility (Grenoble, France). Fig. 2 shows the setup used for the experiments. The monochromatic X-ray beam with an energy of 69.52 keV (wavelength of 0.1783 Å) made it possible to obtain diffraction patterns from the bulk material in transmission geometry. A square beam size defined by slits with a dimension of 50×50 µm was chosen in order to illuminate a small number of grains within the cylindrical bar-shaped sample. For this experiment, a two-dimensional CCD detector (FRELON) (Labiche *et al.*, 2007) and a prototype HIZPAD

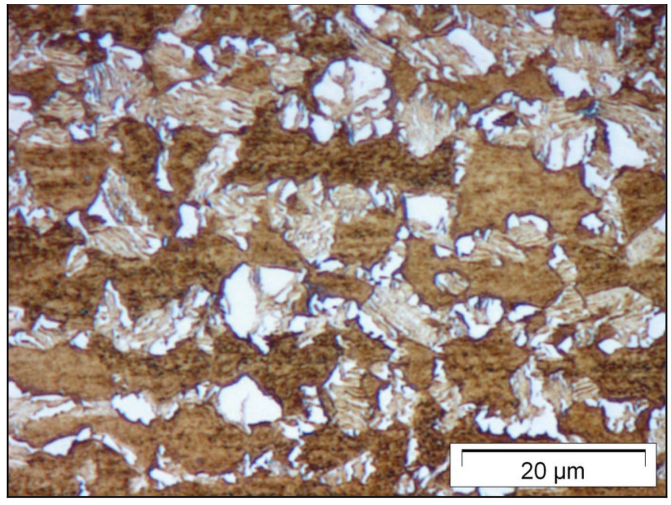

Figure 1
Optical micrograph of the low-alloyed TRIP steel. The room-temperature multiphase microstructure contains a metastable austenite phase (white) within a matrix of ferrite (dark brown) and bainite (light brown) phases.

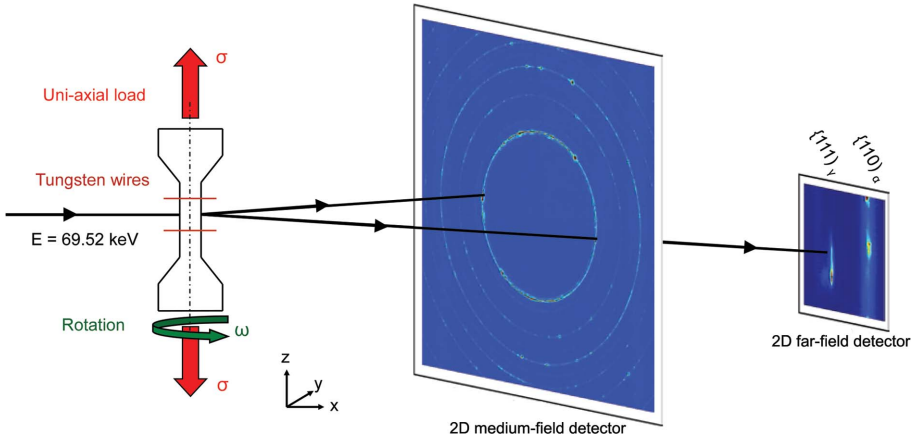

Figure 2
Schematic representation of the setup used for the high-energy microbeam X-ray diffraction experiments in transmission geometry. Two separate two-dimensional (2D) detectors were used: a medium-field CCD detector and a far-field CdTe pixel detector. The sample was under a tensile stress (σ) and continuously rotated around the vertical axis during exposure.

1 mm CdTe pixel detector with 256 × 256 pixels covering an area of 14 × 14 mm (Ruat & Ponchut, 2012) were placed behind the sample at 251.619 and 3239.136 mm, respectively.

2.3. Experimental procedure

To study the mechanical stability of retained austenite, the sample was mounted on a 2 kN micro tensile tester placed on a Huber diffractometer that allowed ω rotations around the cylindrical axis of the sample. For each deformation step the strain was held constant during a complete set of X-ray diffraction measurements, where the diffracted beam was recorded consecutively on both detectors. After each deformation step the sample alignment was checked using the reflection of an untransforming ferrite grain within the illuminated sample volume. For the medium-field (MF) detector data, the sample was continuously rotated during exposure around the cylindrical axis of the sample (perpendicular to the X-ray beam) in steps of 0.2° covering an angular range of 90°. For the far-field (FF) detector data, the $\{111\}_\gamma$ reflection of austenite (face-centred cubic structure) and the $\{110\}_\alpha$ reflection of ferrite (body-centred cubic structure) were monitored simultaneously in the horizontal scattering plane. During the experiments, four individual austenite peaks on the $\{111\}_\gamma$ ring were selected from the MF X-ray diffraction data. These grains were selected by first creating a two-dimensional map of the $\{111\}_\gamma$ ring intensity collected using a vertical translation of the FF detector, covering an angular range of about 1°, combined with a sample rotation of 6°. From this two-dimensional map of the $\{111\}_\gamma$ ring intensity the four most intense austenite reflections located in the central part of the two-dimensional map were selected. The selected peaks were monitored at high resolution using the same method as was adopted with the MF detector but employing smaller rotation steps of 0.002° and covering an angle range between 0.8 and 2.8°, depending on the peak studied. The long sample-to-detector distance for the FF detector allowed us to separate the $\{111\}_\gamma$ and $\{110\}_\alpha$ reflections, which are overlapping on the MF detector.

Assuming an average austenite grain radius of about 3 µm and a transforming blocky-type austenite phase fraction of $f \simeq 3\%$ (these are the largest grains), the expected number of austenite grains within the illuminated sample volume of 50 × 50 × 1000 µm is $N \simeq 700$. These grains will produce $2m_{hkl}N \simeq 8400$ reflections on the $\{111\}_\gamma$ austenite ring, where m_{hkl} is the multiplicity factor of the ring. The average solid angle per reflection, $\Delta\Omega \simeq 4\pi/8400$, results in an angular spacing between the 111 austenite reflections of $(180/\pi)\Delta\Omega^{1/2} \simeq 2°$. This average angular spacing is sufficient to obtain clearly distinguishable individual peaks. The corresponding number of grains that are placed in the central volume that remains illuminated for all sample rotations (10^5 µm^3) is about 30.

Fig. 3(*a*) displays a two-dimensional diffraction pattern of TRIP steel from the MF detector. From this diffraction pattern, the $\{111\}_\gamma$, $\{200\}_\gamma$, $\{220\}_\gamma$ and $\{311\}_\gamma$ austenite reflections have been studied. Each austenite diffraction ring consists of a number of single spots originating from individual austenite grains in the TRIP microstructure, together with a powder signal stemming from austenite grains whose volume falls below the experimental detection limit of about 5 µm^3 for individual grains (Jimenez-Melero *et al.*, 2007*a*). Fig. 3(*b*) shows a high magnification of the region of interest on the MF detector (the resolution is around 0.007 Å^{-1}) and Fig. 3(*c*) is the corresponding XRD pattern for the same grain monitored

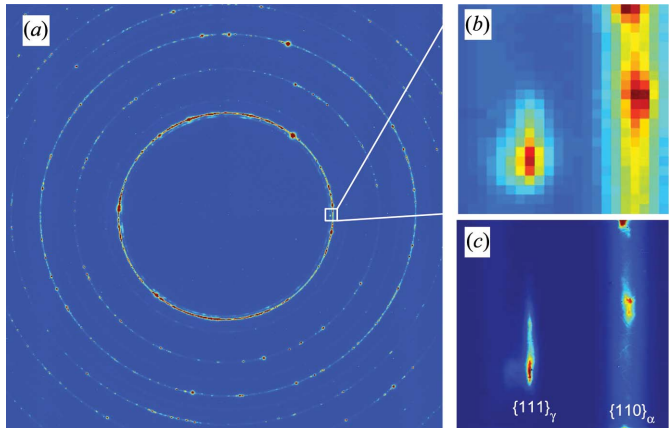

Figure 3
Two-dimensional X-ray diffraction pattern of the TRIP sample. The pattern monitored on the medium-field detector (*a*) shows both ferrite and austenite reflections on separate diffraction rings. (*b*) A zoom of the medium-field data that shows a single austenite diffraction peak from the $\{111\}_\gamma$ ring and part of the $\{110\}_\alpha$ ring of ferrite. (*c*) The corresponding image monitored on the far-field detector provides a higher resolution.

on the FF detector. The longer sample-to-detector distance provides a higher resolution of 0.0006 $Å^{-1}$. The image obtained from the FF detector permits us to evaluate the subgrain structure within an individual austenite grain. The instrumental parameters of the three-dimensional X-ray diffraction microscope for both detectors were determined using a CeO_2 calibrant.

Fig. 4 shows the one-dimensional XRD patterns of CeO_2, resulting from an integration over the azimuthal angles at constant scattering angle of the two-dimensional XRD images measured on the MF and FF detectors. The 2θ values measured on the MF detector range up to 10.7°, while a single image on the CdTe detector covers only 0.25°. The FF detector has been translated horizontally to monitor a range from 5.248 to 8.913° in order to cover six CeO_2 reflections. The FWHM of the 311 reflection determined from a pseudo-Voigt profile fitting decreases from 0.0382 (2) to 0.004903 (3)° for an increasing sample-to-detector distance, corresponding to a decrease in resolution from 6.10 (3) $\times$ 10^{-3} to 7.845 (5) $\times$ 10^{-4}. Changes in the sample-to-detector distance during straining were determined using a CeO_2 calibrant placed on the sample.

3. Data analysis

3.1. Powder data analysis

The wide ω angle range monitored on the MF detector was used to perform an accurate powder XRD data analysis. The measured data consisted of a series of two-dimensional diffraction patterns as a function of sample elongation and ω angle. The two-dimensional diffraction patterns for the complete ω range covered in this experiment were summed. Afterwards, an integration over the azimuthal angles at constant scattering angle was performed using the *FIT2D* software package (Hammersley *et al.*, 1996) to obtain the corresponding one-dimensional diffraction patterns at different strain steps. A Rietveld refinement of the resulting one-dimensional X-ray diffraction patterns was performed using the *Fullprof* package (Rodríguez-Carvajal, 1993) in order to determine the phase fraction and lattice parameter of the constituent phases as a function of the macroscopic strain.

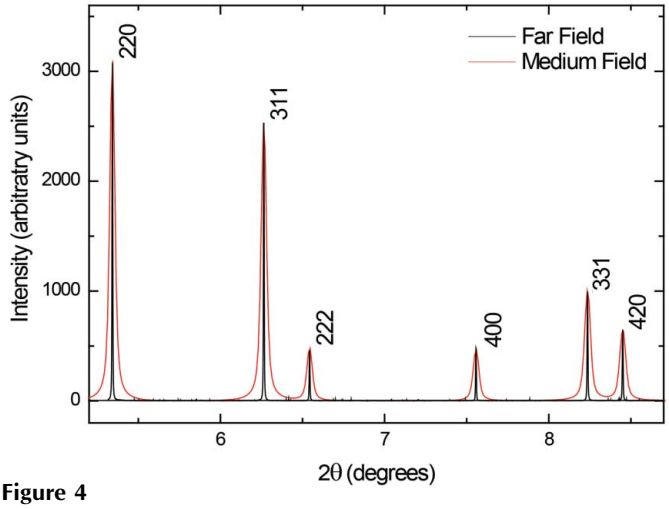

Figure 4
One-dimensional X-ray diffraction patterns of the CeO_2 calibrant measured with both detectors.

3.2. Data analysis of single grains on the medium-field detector

The volume, crystallographic orientation, centre-of-mass position and strain state of the four monitored individual grains have been determined. For the data analysis the algorithms recently developed by Sharma *et al.* (2012*a*,*b*) were applied. The first step consisted of a peak search of the austenite peaks, where the detection threshold was scaled with the structure factor of the studied (*hkl*) plane because of their relatively weak intensity. The next step consisted of the assignment of diffraction spots to individual grains and refining them to obtain accurate values. The volume of a grain was obtained from the integrated intensities of the corresponding diffraction spots. Full grain illumination was checked by evaluation of the grain position from the reflections on the MF detector.

3.3. Data analysis of single grains on the far-field detector

The grain volume V_g of the four monitored diffraction peaks was determined from the integrated intensity I_g of the single grain reflection on the FF detector by a scaling to the powder intensity of the corresponding diffraction ring I_p on the MF detector:

$$V_g = \tfrac{1}{2} m_{hkl} \Delta\omega \cos(\theta) f^{\gamma} V_{\text{gauge}} I_g / I_p, \qquad (1)$$

where $\Delta\omega$ is the angular range over which the grain is rotated, f^{γ} is the volume fraction of the austenite phase determined from the powder data analysis from the MF data, and V_{gauge} is the gauge volume, which is defined by the beam size and the thickness of the sample.

4. Results and discussion

4.1. Macroscopic mechanical behaviour

Fig. 5(*a*) shows the macroscopic (engineering) stress–strain curve of the low-alloyed TRIP steel. Two tungsten wires glued onto the surface of the sample perpendicular to the loading direction acted as an accurate strain gauge during deformation. Each data point on the curves represents a set of X-ray diffraction measurements while the macroscopic strain is held constant. We recorded the diffraction patterns for a series of elongation steps up to the yield strength. The stress–strain data provided a yield strength of 425 MPa and an ultimate tensile strength of 624 MPa at strain levels of 0.83 and 5.95%, respectively. These values are in good agreement with values obtained on macroscopic samples.

4.2. Austenite phase fraction evolution

A powder analysis of the XRD data indicated an austenite volume fraction of 8.5 (3)% at room temperature. By

increasing the macroscopic strain, the mechanically induced transformation starts well before the macroscopic yield stress is reached. The fraction decreases continuously to 5.6 (2)% for strains up to 0.8% and then remains roughly constant until the maximum applied strain (see Fig. 5*b*).

4.3. Single-grain analysis

The four reflections monitored on the FF detector were tracked back to the MF diffraction data. For the four individual grains of interest, a collection of austenite peaks on different diffraction rings were identified and indexed to obtain the grain orientation. The grain volume, the lattice parameter and the derived carbon concentration of the four indexed grains at zero deformation are reported in Table 2. The relation between the austenite lattice parameter and the grain's chemical composition is given by (van Dijk *et al.*, 2005; Scott & Drillet, 2007)

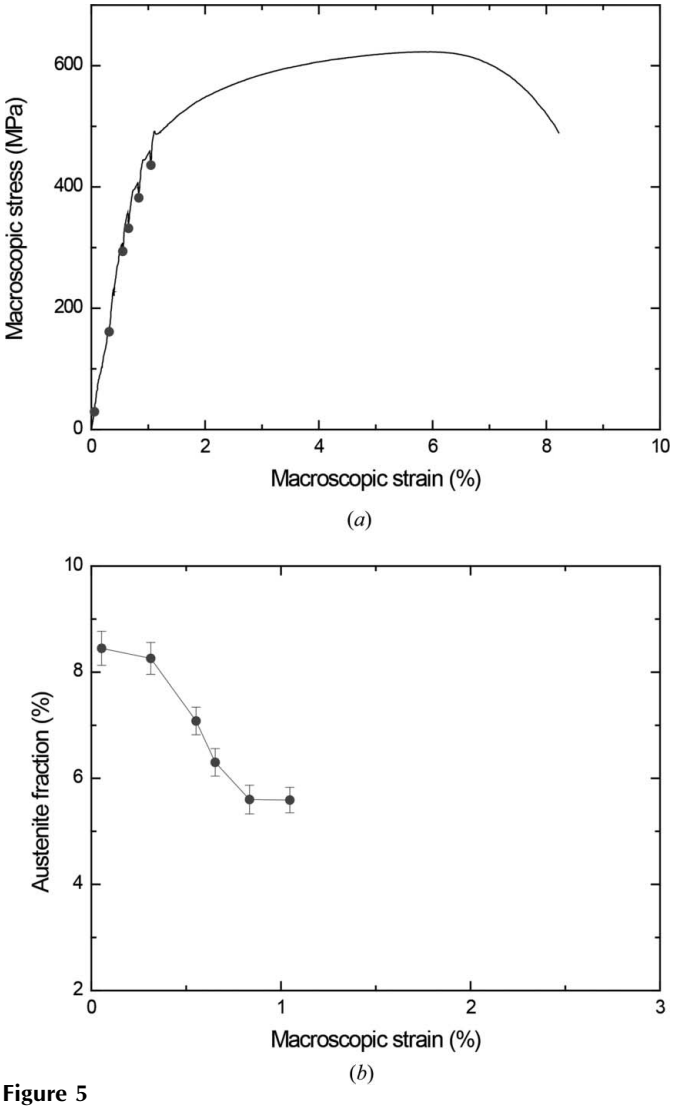

Figure 5
(*a*) Macroscopic (engineering) stress–strain curves of TRIP steel measured stepwise during the *in situ* X-ray diffraction experiments and (*b*) the austenite fraction as a function of the macroscopic strain.

Table 2
Grain characteristics for the four grains studied on the medium-field detector before deformation.

Grain	Lattice parameter (Å)	Carbon concentration (wt%)
1	3.6015 (1)	0.757 (2)
2	3.6039 (1)	0.809 (2)
3	3.6031 (1)	0.791 (2)
4	3.6120 (1)	0.987 (2)

$$a_\gamma = 3.556 + 0.0453x_C + 0.00095x_{Mn} + 0.0056x_{Al}, \quad (2)$$

where a_γ is the austenite lattice parameter in Å and x_C, x_{Mn} and x_{Al} are the alloying concentrations in wt%. The presence of Si and P is considered to have a negligible effect on the lattice parameter of austenite. The studied grains are blocky-type austenite grains, which constitute the remaining parts of the intercritical austenite grains after the partial bainitic transformation. Both the carbon enrichment and the grain volume are significant parameters to retain the austenite stability at room temperature. These microstructural parameters have been intensively investigated to establish their relation to the martensitic start temperature of the austenite-to-martensite transformation (Jimenez-Melero *et al.*, 2007*a*,*b*, 2009; van Dijk *et al.*, 2005):

$$M_s = M_{so} - Ax_c - BV_\gamma^{-1/3}. \quad (3)$$

The first two terms of this expression reflect the well known Andrews empirical relation between the martensitic start temperature, M_s, and the carbon content, with A = 425 K wt%$^{-1}$ (Andrews, 1965), while the third term was recently introduced to quantify the effect of the grain volume on its stability. M_{so} = 702 K and B = 475 µm K for the current TRIP microstructure (Jimenez-Melero *et al.*, 2007*a*).

The derived grain orientation was used to map the tensile direction in the inverse pole figure represented by the stereographic triangle in Fig. 6. The background colour in the

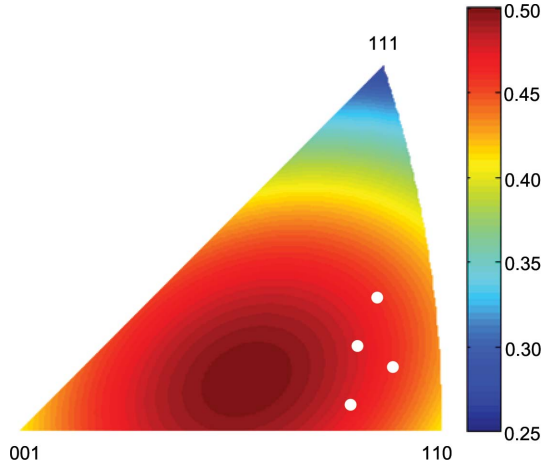

Figure 6
Stereographic triangle representing the grain orientation with respect to the loading direction at no deformation. The white spheres indicate the relative orientation of the four grains studied. The colour scheme represents the theoretical Schmid factor for the most favourable slip system in a face-centred cubic system.

inverse pole figure corresponds to the theoretical Schmid factor for a face-centred cubic system. The Schmid factor represents the relative strength of the maximum resolved shear stress along the relevant slip system that drives the austenite-to-martensite transformation. The four selected grains exhibit a Schmid factor of about 0.45, which is close to the highest theoretical value of 0.5.

Table 3
Grain characteristics for the four grains studied on the far-field detector before deformation.

Q_0 (Å^{-1})	$\langle q_{par}^2\rangle^{1/2}$ (10^{-3} Å^{-1})	$\langle q_{perp}^2\rangle^{1/2}$ (10^{-3} Å^{-1})	$\langle\Delta 2\theta\rangle$ (°)	$\langle\Delta\alpha\rangle$ (°)	$\langle\varepsilon^2\rangle^{1/2}$ (%)	Volume (µm^3)	Radius (µm)	Subgrains (number)
3.0248	0.7056	12.463	0.0011	0.0035	0.023	1426	6.98	1066
3.0248	0.9096	6.175	0.0015	0.0011	0.030	369.3	4.45	263
3.0260	3.3801	52.414	0.0055	0.0150	0.112	658.1	5.40	422
3.0243	1.0271	5.679	0.0017	0.0014	0.034	251.1	3.91	82

4.4. High-resolution data analysis

The integrated radial peak profile was fitted with a pseudo-Voigt function, and the resulting parameters for the four austenite grains are reported in Table 3. Fig. 7 shows the projection of the two-dimensional intensity distribution onto the plane Q_xQ_z perpendicular to the scattering vector at no deformation. This two-dimensional projection of the three-dimensional diffraction peaks in reciprocal space shows a complex variation in the diffracted intensity originating from a single grain. For grain 1, it is clearly observed that the peak consists of one central peak with a rich substructure. In high resolution the pronounced substructure of the reflection is observed even before applying any macroscopic tensile load. Several small sharp peaks, slightly misoriented with respect to the main peak, are observed, indicating the presence of subgrains within the grain. The presence of a rich dislocation structure within the austenite grain before applying a tensile deformation may find its origin in the TRIP heat treatment, where a certain number of dislocations are expected be induced by the bainite formation and the resulting inhomogeneous residual stresses. Such a pre-existing substructure has been observed for all four grains. For grain 3, besides the central peak, a disconnected more diffuse contribution is observed. It cannot be excluded that the intensity of the diffuse contribution in Fig. 7 (lower left) originates from a different grain. However, the 111 austenite reflections are generally well separated under the current conditions. An alternative explanation is that during the bainitic transformation in a limited number of cases two spatially separated units originating from the same grain are generated (Jimenez-Melero *et al.*, 2007*a*). In this case these retained austenite units can have a slightly different orientation.

To obtain a better insight into the substructure representing the dislocation network, each subpeak with a local maximum in intensity within the three-dimensional peak profile presented in Fig. 7 was studied independently and compared with the centre of mass of the total reflection. The scattering vectors $\mathbf{Q}$ of each subpeak and $\mathbf{Q}_0$ of the full peak were compared. In Fig. 8, the resulting difference vector $\mathbf{q} = \mathbf{Q} - \mathbf{Q}_0 = \mathbf{q}_{par} + \mathbf{q}_{perp}$ has been decoupled into $\mathbf{q}_{par}$ and $\mathbf{q}_{perp}$, corresponding, respectively, to the components along

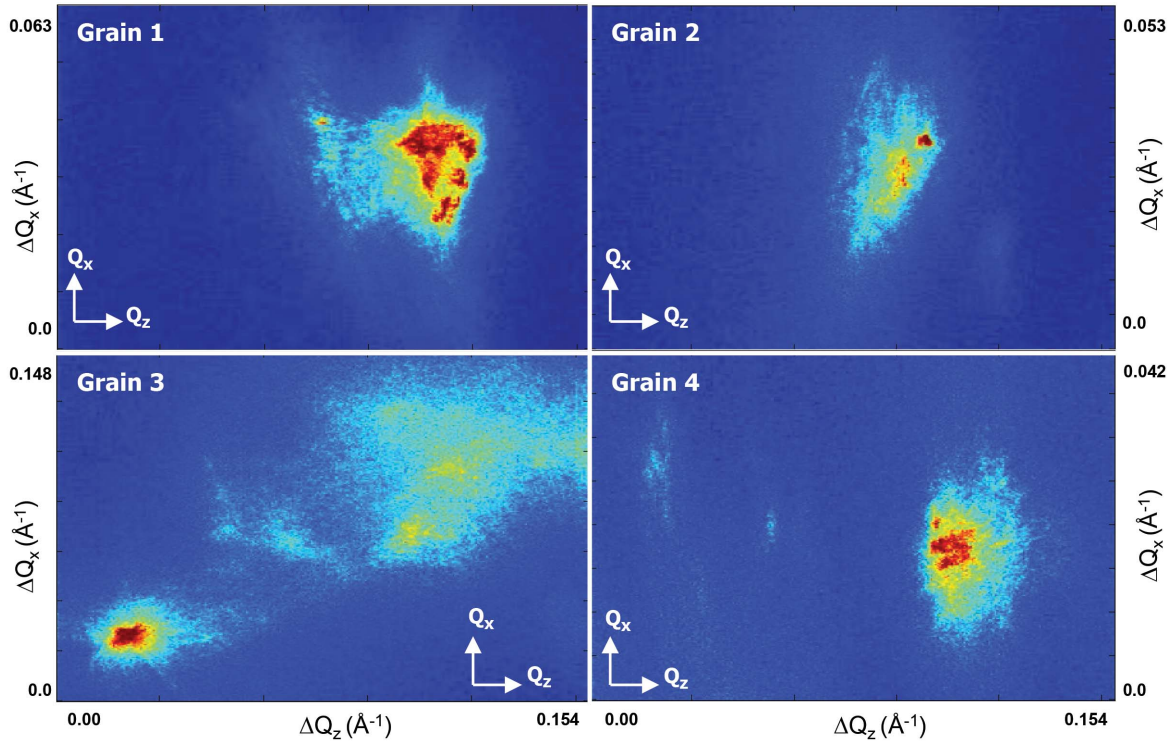

Figure 7
Projection of the three-dimensional reciprocal space intensity distribution onto the azimuthal plane Q_xQ_z at no deformation.

and perpendicular to $\mathbf{Q}_0$. The maximum misorientation for the subpeaks amounts to $\Delta q_{\rm perp} = 0.0336$ Å^{-1}. The variation in lattice parameter, represented by $\Delta q_{\rm par}$, is significantly smaller. In Table 3 the grain volume and the number of assigned subgrains are listed for the studied grains. When the grain volume is divided by the number of identified subgrains an average volume of about 1 µm^3 is obtained for all four grains. This value should be regarded as an upper bound for the average subgrain size, as the smallest subgrains cannot be identified because of the overlap of subgrain diffraction peaks: the weakest peaks are indistinguishable when they fall inside the tails of the more intense peaks from larger subgrains. The fact that the average subgrain size is significantly smaller than 1 µm is consistent with typical experimental dislocation densities of the order of 10^{14} m^{-2} (Zhao *et al.*, 2005; Zhang *et al.*, 2011), which corresponds to an average subgrain size of about 0.1 µm.

The characteristics of the subgrain structure can be quantified in more detail using an autocorrelation function of the three-dimensional high-resolution peak structure represented in Fig. 7. The correlation function reflects the nature of the spatial correlations within the material (Hähner *et al.*, 1998; Ispánovity *et al.*, 2008; Chen *et al.*, 2013). The used reciprocal-space autocorrelation function corresponds to

$$C(\mathbf{q}) = \frac{\langle I(\mathbf{0})I(\mathbf{q})\rangle}{\langle I(\mathbf{0})I(\mathbf{0})\rangle}, \qquad (4)$$

where $\mathbf{q}$ is the difference vector in reciprocal space and $I(\mathbf{q})$ is its corresponding intensity. The resulting curves for grain 1 are shown in Fig. 9. Two types of contributions are present in the autocorrelation function: a sharp initial decrease in the first displacement step, followed by a smooth continuous decrease. The overall behaviour closely follows an exponential of the following form:

$$C(q_i) = (1-\eta) + \eta \exp\left(-c\left|q_i\right|\right), \qquad (5)$$

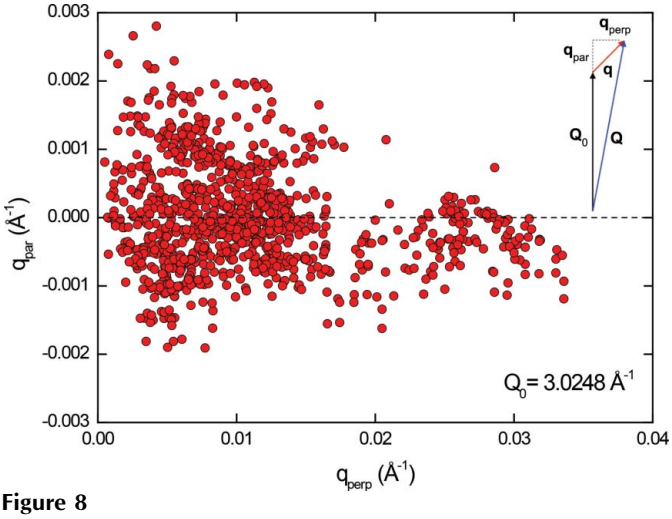

Figure 8
Scattering vectors of the subpeaks of grain 1. The scattering vector is $\mathbf{Q} = \mathbf{Q}_0 + \mathbf{q}$, decomposed into the central vector $\mathbf{Q}_0$ and the deviatory vector $\mathbf{q}$. The vector $\mathbf{q}$ is decomposed into components $q_{\rm par}$ along and $q_{\rm perp}$ perpendicular to $\mathbf{Q}_0$, respectively.

where q_i is the component of $\mathbf{q}$ along ($q_{\rm par}$) and perpendicular ($q_{\rm perp}$) to $\mathbf{Q}_0$. This autocorrelation function reflects a Lorentzian distribution $(1/\pi)\{(\Gamma/2)/[x^2 + (\Gamma/2)^2]\}$ for a symmetric real-space displacement x with a full width at half-maximum Γ (Vermeulen *et al.*, 1995). The constant c is linked to the distribution by $c = \pi\Gamma$. In our case the constant c has been calculated in both dimensions: $c_{\rm perp} = 70.6\ (2)$ Å and $c_{\rm par} = 33.2\ (5)$ Å. The corresponding correlation distance for the displacement fields is as low as $\Gamma_{\rm par} \simeq 1$ nm. This confirms earlier observations that the subgrains within a single grain form a hierarchical structure with characteristic sizes ranging from the nanometre up to the micrometre range (Hähner *et al.*, 1998; Ispánovity *et al.*, 2008).

4.5. Strain effect on the substructure of individual austenite grains

Fig. 10 shows a projection of the three-dimensional diffraction peak of grain 4 for both detectors as a function of

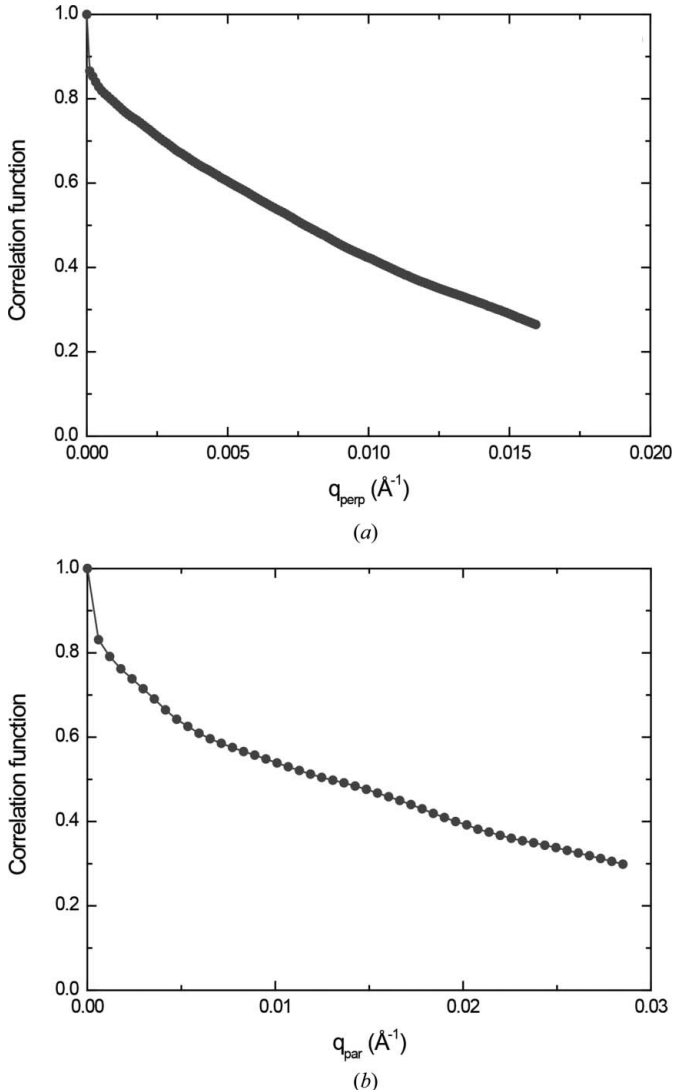

Figure 9
Correlation function of the two-dimensional peak of grain 1 as a function of (*a*) $q_{\rm perp}$ and (*b*) $q_{\rm par}$.

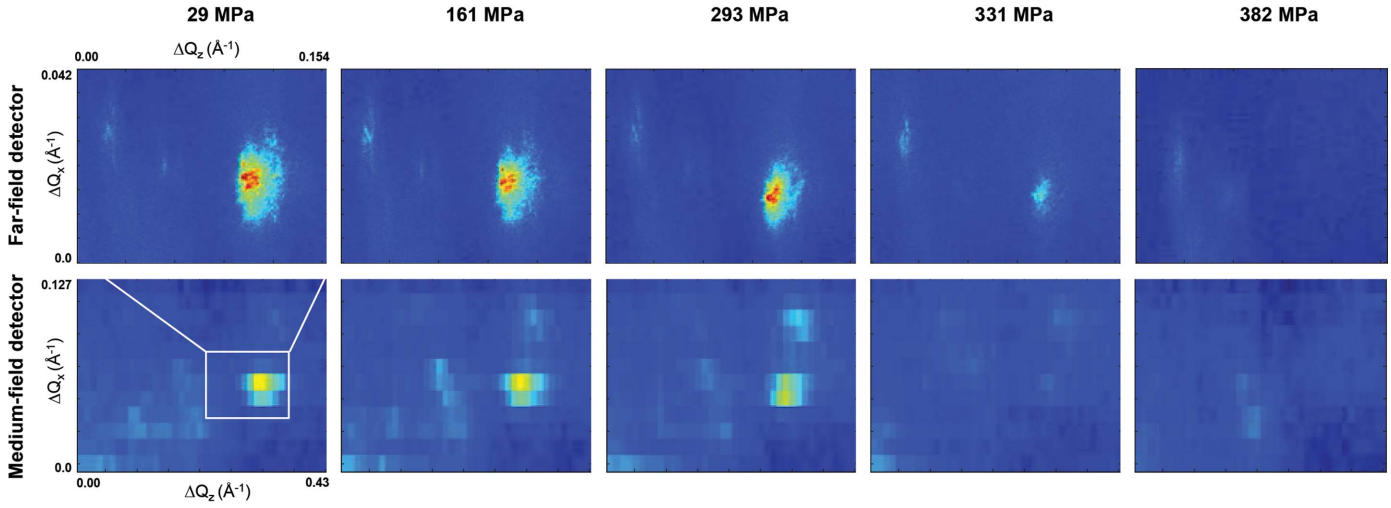

Figure 10
Projection of the three-dimensional reciprocal-space intensity distribution of grain 4 onto the azimuthal plane Q_xQ_z. A series of projections for both detectors and for five stress states is presented.

the stress state. The sequence illustrates the power of high-resolution diffraction to study the evolution in subgrain structure during tensile deformation (Pantleon *et al.*, 2009). It is observed (on both detectors) that the single-grain reflection remains essentially unchanged for increasing strain levels well below the macroscopic yield strength until a critical stress is reached and the reflection disappears. The tensile load required for macroscopic yielding to induce plastic deformation is not reached at this stage. The reason the peak intensity disappeared for 382 MPa is that the critical stress level to activate the martensitic transformation has been reached. As shown in Fig. 10, the high-resolution data indicate that the peak position is only weakly affected by the tensile load. In the macroscopic elastic regime the grains, embedded in the multiphase microstructure, are indeed not expected to show a significant rotation.

Even though this may not be anticipated, it is important to check that the disappearance of the austenite reflection originates from a martensitic transformation and is not caused by a sudden grain rotation (potentially caused by the transformation of a neighbouring austenite grain). This cannot be excluded from the limited angular view probed by the FF detector. Therefore, the MF data were used to index multiple peaks originating from the same grain. Using the 3DXRD method (Sharma *et al.*, 2012*a*,*b*), the orientation matrix of the four individual grains was obtained for each deformation step from the combined set of reflections collected on the MF detector over a wide angular rotation range. The grain orientation of the four grains was tracked for increasing stress. The resulting stereographic projection was found to be equivalent to the initial representation shown in Fig. 6. No grain rotation has been observed in the macroscopic elastic regime for the four grains of interest.

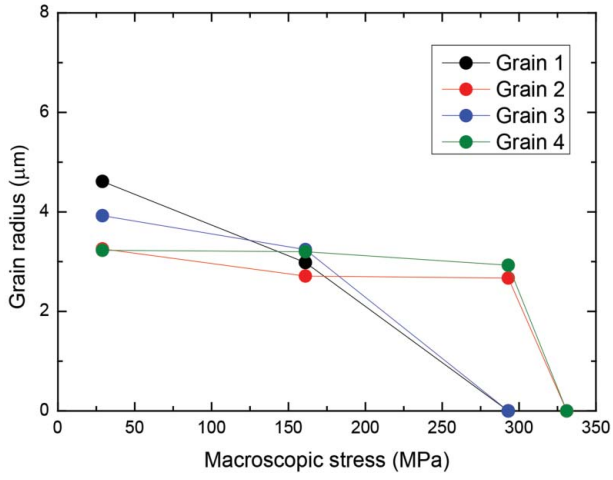

Figure 11
Grain volume as a function of the applied macroscopic stress from the medium-field single-grain data analysis.

As explained in a previous study on thermal stability (Jimenez-Melero *et al.*, 2007*a*,*b*), different types of transformation behaviour exist: (i) no transformation, (ii) a complete transformation (in a single cooling step) and (iii) a partial transformation (in more than one cooling step). Under tensile deformation we find that most grains show a complete martensitic transformation in a single strain step. In Fig. 11, the grain volume as a function of the macroscopic strain is presented. Grains 2–4 transformed in one step, while grain 1 shows a partial transformation in the first step. The grain volume reduced significantly in the first strain step and disappeared in the second strain step.

5. Conclusions

We have performed *in situ* high-resolution X-ray diffraction experiments at a synchrotron source in order to obtain a full characterization of individual metastable austenite grains within a multiphase TRIP microstructure. A multi-method approach focusing on the phase averages (powder data), single grains (microbeam data) and subgrains (high-resolution data) has been followed. The main conclusions are as follows: (1)

The presented method of using a far-field detector allows us to study individual Bragg reflections at high resolution. This makes it possible to resolve subgrains in austenite grains prior to the martensitic transformation. (2) We have observed that the austenite grains already contain a pronounced initial substructure before any mechanical load has been applied. The corresponding dislocations are expected to be the result of local transformation strains during the TRIP heat treatment. (3) Austenite grains have been tracked during tensile deformation at stress level lower than the macroscopic yield stress. Most austenite grains show a complete martensitic transformation in a single strain step. (4) A full grain characterization from the medium-field data shows that the grains do not rotate before reaching the required critical resolved shear stress for transformation.

This research was carried out under the project number M41.5.08313 in the framework of the Research Program of the Materials innovation institute M2i (http://www.m2i.nl). We acknowledge the European Synchrotron Radiation Facility for provision of synchrotron radiation facilities and thank the beamline staff for assistance in using beamline ID11 and particularly M. Ruat for assistance with the CdTe detector.

References

Andrews, K. J. (1965). *J. Iron Steel Inst.* **203**, 721–727.
Bernier, J. V., Barton, N. R., Lienert, U. & Miller, M. P. (2011). *J. Strain Anal. Eng.* **46**, 527–547.
Blondé, R., Jimenez-Melero, E., van Dijk, N. H., Brück, E., Zhao, L., Sietsma, J. & van der Zwaag, S. (2011). *Solid State Phenom.* **196**, 172–174.
Blondé, R., Jimenez-Melero, E., Zhao, L., Wright, J., Brück, E., van der Zwaag, S. & van Dijk, N. (2012). *Acta Mater.* **60**, 565–577.
Chen, Y. S., Choi, W., Papanikolaou, S., Bierbaum, M. & Sethna, J. P. (2013). *Int. J. Plast.* **46**, 94–129.
Dalla Torre, F., Lapovok, R., Sandlin, J., Thomson, P., Davies, C. & Pereloma, E. (2004). *Acta Mater.* **52**, 4819–4832.
Dan, W., Zhang, W., Li, S. & Lin, Z. (2007). *Comput. Mater. Sci.* **40**, 101–107.
Dijk, N. H. van, Butt, A. M., Zhao, L., Sietsma, J., Offerman, S. E., Wright, J. P. & van der Zwaag, S. (2005). *Acta Mater.* **53**, 5439–5447.
Edmiston, J. K., Barton, N. R., Bernier, J. V., Johnson, G. C. & Steigmann, D. J. (2011). *J. Appl. Cryst.* **44**, 299–312.
Hähner, P., Bay, K. & Zaiser, M. (1998). *Phys. Rev. Lett.* **84**, 2470–2473.
Hammersley, A. P., Svensson, S. O., Hanfland, M., Fitch, A. N. & Hausermann, D. (1996). *High Pressure Res.* **14**, 235–248.
Huang, J., Zhu, Y., Jiang, H. & Lowe, T. (2001). *Acta Mater.* **49**, 1497–1505.
Humphreys, F. J. (2001). *J. Mater. Sci.* **36**, 3833–3854.
Ispánovity, P., Groma, I. & Györgyi, G. (2008). *Phys. Rev. B*, **78**, 024119.
Jacques, P., Furnémont, Q., Lani, F., Pardoen, T. & Delannay, F. (2007). *Acta Mater.* **55**, 3681–3693.
Jakobsen, B., Poulsen, H. F., Lienert, U., Almer, J., Shastri, S. D., Sørensen, H. O., Gundlach, C. & Pantleon, W. (2006). *Science*, **312**, 889–892.
Jakobsen, B., Poulsen, H. F., Lienert, U. & Pantleon, W. (2007). *Acta Mater.* **55**, 3421–3430.
Jiang, J., Britton, T. & Wilkinson, A. (2013). *Acta Mater.* **61**, 7227–7239.
Jimenez-Melero, E., van Dijk, N. H., Zhao, L., Sietsma, J., Offerman, S. E., Wright, J. P. & van der Zwaag, S. (2007*a*). *Scr. Mater.* **56**, 421–424.
Jimenez-Melero, E., van Dijk, N. H., Zhao, L., Sietsma, J., Offerman, S. E., Wright, J. P. & van der Zwaag, S. (2007*b*). *Acta Mater.* **55**, 6713–6723.
Jimenez-Melero, E., van Dijk, N., Zhao, L., Sietsma, J., Offerman, S., Wright, J. & van der Zwaag, S. (2009). *Acta Mater.* **57**, 533–543.
Jimenez-Melero, E., van Dijk, N., Zhao, L., Sietsma, J., Wright, J. & van der Zwaag, S. (2011). *Mater. Sci. Eng. A*, **528**, 6407–6416.
Labiche, J., Mathon, O., Pascarelli, S., Newton, M. A., Ferre, G. G., Curfs, C., Vaughan, G., Homs, A. & Carreiras, D. F. (2007). *Rev. Sci. Instrum.* **78**, 091301.
Militzer, M. (2002). *Science*, **298**, 975–976.
Oddershede, J., Schmidt, S., Poulsen, H. F., Sørensen, H. O., Wright, J. & Reimers, W. (2010). *J. Appl. Cryst.* **43**, 539–549.
Pantleon, W., Wejdemann, C., Jacobsen, B., Lienert, U. & Poulsen, H. F. (2009). *Mater. Sci. Eng. A*, **524**, 55–63.
Poulsen, H. F. (2004). *Three-Dimensional X-ray Diffraction Microscopy – Mapping Polycrystals and Their Dynamics*. Heidelberg: Springer.
Rodríguez-Carvajal, J. (1993). *Physica B*, **192**, 55–69.
Ruat, M. & Ponchut, C. (2012). *IEEE Trans. Nucl. Sci.* **59**, 2392–2401.
Schmidt, S., Poulsen, H. F. & Vaughan, G. B. M. (2003). *J. Appl. Cryst.* **36**, 326–332.
Scott, C. & Drillet, J. (2007). *Scr. Mater.* **56**, 489–492.
Sharma, H., Huizenga, R. M. & Offerman, S. E. (2012*a*). *J. Appl. Cryst.* **45**, 693–704.
Sharma, H., Huizenga, R. M. & Offerman, S. E. (2012*b*). *J. Appl. Cryst.* **45**, 705–718.
Timokhina, I. B., Hodgson, P. D. & Pereloma, E. V. (2004). *Metall. Mater. Trans. A*, **35**, 2331–2341.
Vermeulen, A. C., Delhez, R., de Keijser, T. H. & Mittemeijer, E. J. (1995). *J. Appl. Phys.* **77**, 5026–5049.
Zaefferer, S., Ohlert, J. & Bleck, W. (2004). *Acta Mater.* **52**, 2765–2778.
Zhang, K., Zhang, M., Guo, Z., Chen, N. & Rong, Y. (2011). *Mater. Sci. Eng. A*, **528**, 8486–8491.
Zhao, L., van der Pers, N., Sietsma, J. & van der Zwaag, S. (2005). *Mater. Sci. Forum*, **500–501**, 379–386.